REPORT

ELECTROCHEMISTRY

CO_2 electrolysis to multicarbon products at activities greater than 1 A cm^{-2}

F. Pelayo García de Arquer[1]*, Cao-Thang Dinh[1]*, Adnan Ozden[2]*, Joshua Wicks[1,3]*, Christopher McCallum[2], Ahmad R. Kirmani[4], Dae-Hyun Nam[1], Christine Gabardo[2], Ali Seifitokaldani[1], Xue Wang[1], Yuguang C. Li[1], Fengwang Li[1], Jonathan Edwards[2], Lee J. Richter[4], Steven J. Thorpe[3], David Sinton[2]†, Edward H. Sargent[1]†

Electrolysis offers an attractive route to upgrade greenhouse gases such as carbon dioxide (CO_2) to valuable fuels and feedstocks; however, productivity is often limited by gas diffusion through a liquid electrolyte to the surface of the catalyst. Here, we present a catalyst:ionomer bulk heterojunction (CIBH) architecture that decouples gas, ion, and electron transport. The CIBH comprises a metal and a superfine ionomer layer with hydrophobic and hydrophilic functionalities that extend gas and ion transport from tens of nanometers to the micrometer scale. By applying this design strategy, we achieved CO_2 electroreduction on copper in 7 M potassium hydroxide electrolyte (pH ≈ 15) with an ethylene partial current density of 1.3 amperes per square centimeter at 45% cathodic energy efficiency.

The electrochemical transformation of gases into value-added products using renewable energy is an attractive route to upgrade CO_2 and CO into fuels and chemical feedstocks (*1*–*4*) based on hydrocarbons. The success of the approach will rely on continued improvements in energy efficiency to minimize operating costs and on increasing current density to minimize capital costs (*5*, *6*). This will require catalysts that facilitate adsorption, coupling, and hydrogenation via proton-coupled electron transfer steps (*7*–*9*).

In these reactions, water-based electrolytes act both as a proton source and as the ion conductive medium (*10*). However, the solubility of these gases in water is limited, leading to constrained gas diffusion as gas molecules collide or react with their environment (*11*). The diffusion length of CO_2 can be as low as tens of nanometers in alkaline aqueous environments (*12*). This has limited the productivity of catalysts in aqueous cells to current densities in the range of tens of milliamperes per square centimeter due to mass transport (*13*–*16*).

In a gas-phase electrolyzer, catalyst layers are deposited onto hydrophobic gas-diffusion layers so that gas reactants need to diffuse only short distances to reach electroactive sites on the catalyst surface (Fig. 1A) (*17*–*19*). Gas reactant diffusion in the catalyst layer becomes the mass transport–limiting step in the cathode, as observed in the oxygen reduction reaction (ORR) in fuel cells. To improve ORR performance, fuel-cell catalyst layers are designed to balance hydrophobicity to help expel water and hydrophilicity to maintain sufficient ion conductivity.

In contrast with oxygen reduction, which generates water as a product, CO_2 reduction requires water as a proton source for hydrocarbon production. Thus, the catalyst layer is hydrophilic and fully hydrated during the reaction. In this configuration, CO_2 electrochemical reactions occur within a gas-liquid-solid three-phase reaction interface (Fig. 1B) (*20*). This volume, in which gaseous reactants and electrolytes coexist at catalyst electroactive sites, decays rapidly into the electrolyte, particularly at the high pH used in alkaline electrolysis. The decay is further increased at high current densities because of local OH^- generation (*21*). A large fraction of the catalyst is in contact with electrolyte in which CO_2 availability is limited by its solubility (<2 mM at pH 15). Because hydrogen evolution is a competing reaction with CO_2 reduction in a similar applied potential range, the large fraction of catalyst surface area exposed to CO_2-depleted electrolyte promotes undesired H_2 generation (Fig. 1C). Whereas recent advances in gas-phase CO_2 reduction have led to partial current densities for CO_2 reduction of ≈100 mA cm^{-2} (*12*, *22*, *23*), other liquid-phase electrochemical technologies such as water electrolysis achieve multi-amperes per square centimeter (*24*, *25*).

High-temperature solid oxide electrolysis offers a strategy to achieve CO_2 reduction at high current density: CO_2 diffuses directly to the surface of the catalyst, in the absence of liquid electrolyte, thus overcoming the gas diffusion limitations of low-temperature systems. However, high-temperature conditions and the absence of liquid electrolyte have thus far limited CO_2 reduction to the production to CO (*26*).

Here, we present a hybrid catalyst design that, by decoupling gas, ion, and electron transport, enables efficient CO_2 and CO gas-phase electrolysis at current densities in the >1–A cm^{-2} regime to generate multicarbon products. We exploit an ionomer layer that, with hydrophobic and hydrophilic functionalities, assembles into a morphology with differentiated domains that favor gas and ion transport routes, conformally, over the metal surface: Gas transport is promoted through a side chain of hydrophobic domains, leading to extended gas diffusion, whereas water uptake and ion transport occur through hydrated hydrophilic domains (Fig. 1D). As a result, the reaction interface at which these three components come together—gaseous reactants, ions, and electrons—all at catalytically active sites, is increased from the submicrometer regime to the several micrometer length scale.

We began by modeling the available gaseous reactant in different gas-phase electrolysis scenarios (Fig. 1, E and F), building on previously established models (*27*) (see methods for more details). We explored how catalyst performance toward gas electroreduction would be modified as the availability of the gas reactant varied at the gas-electrolyte interface. To do so, we introduced an intermediate surface channel of 20-nm thickness between the catalyst and the electrolyte with an in-plane gas diffusion coefficient (D) appreciably different from that of bulk electrolyte (D_0). As D/D_0 increases, gas flow is promoted through this layer until the gas is converted at the catalyst surface or diffuses into the electrolyte (Fig. 1F), potentially enabling CO_2 diffusion on the scale of several micrometers; whereas, for a standard catalyst configuration, CO_2 is available only within about 1 μm (Fig. 1E). As the diffusion in the layer increases, so too does the current available for the electrochemical conversion of the gas reactant (Fig. 1G). A similar trend holds for other reactant gases such as O_2 (fig. S5).

We sought to design and implement such an enhanced transport system experimentally. We turned our attention to perfluorinated sulfonic acid (PFSA) ionomers, which combine hydrophobic and hydrophilic functionalities along with ion transport (*28*–*30*). We hypothesized that their controlled assembly into distinct hydrophobic and hydrophilic layered domains would offer differentiated pathways whereby gas transport is promoted through the hydrophobic domains and water and ion transport are facilitated by the hydrophilic domains (*31*–*36*) (Fig. 2A).

PFSA ionomers such as Nafion contain $-SO_3^-$ (hydrophilic) and $-CF_2$ (hydrophobic) groups.

[1]Department of Electrical and Computer Engineering, University of Toronto, 35 St. George St., Toronto, Ontario M5S 1A4, Canada. [2]Department of Mechanical and Industrial Engineering, University of Toronto, 5 King's College Rd., Toronto, Ontario M5S 3G8, Canada. [3]Department of Materials Science & Engineering (MSE), University of Toronto, 184 College St., Toronto, Ontario M5S 3E4, Canada. [4]Materials Science and Engineering Division, National Institute of Standards and Technology (NIST), Gaithersburg, MD 20899, USA.
*These authors contributed equally to this work.
†Corresponding author. Email: ted.sargent@utoronto.ca (E.H.S.); sinton@mie.utoronto.ca (D.S.)

Nafion, a widely used material in fuel cells as a catalyst binder and membrane material, exhibits strong structure-function–dependent properties (*28*, *37*). In a polar solvent (i.e., methanol), PFSA ionomers form colloids with hydrophilic $-SO_3^-$ groups exposed to solvent (*28*). When this PFSA ionomer solution is coated on the metallic catalyst surface, we expect a configuration in which $-SO_3^-$ is preferentially exposed to hydrophilic polycrystalline metal surfaces and electrolyte provides continuous percolating hydrophobic paths through $-CF_2$ hydrophobic domains (Fig. 2B).

Seeking to promote the exposure of SO_3^- groups toward catalyst and electrolyte surfaces, we prepared ionomer solutions in polar solvents, which we then spray-coated onto hydrophilic metal catalysts deposited on a porous polytetrafluoroethylene (PTFE) substrate at different loadings (*36*, *38*, *39*). The hydrophobicity of the catalysts before and after ionomer modification was characterized using static contact angles: These yielded similar values of ≈121° to 122° (fig. S8). Scanning electron microscopy (SEM) images revealed a homogeneous, conformal ionomer coating over the entire catalyst (Fig. 2, C and D). Cryo-microtomed cross-sectional transmission electron microscopy (TEM) images revealed the presence of a 5- to 10-nm continuous and conformal ionomer layer (Fig. 2, E to G), establishing a catalyst:ionomer planar heterojunction (CIPH).

To characterize the CIPH structural configuration, we carried out wide-angle x-ray scattering (WAXS) measurements on PTFE/Cu/ionomer samples (Fig. 2H and fig. S9). Both reference and CIPH samples exhibited a similar contribution of the different Cu planes and PTFE backbone support. CIPH samples, in addition, revealed weak scattering at 1.2 $Å^{-1}$ from the amorphous PFSA phase. The crystalline PFSA is masked by the PTFE support at 1.28 $Å^{-1}$ (*28*). Attempts to quantify ≈10-nm thin-film ionomers using grazing-incidence WAXS were unsuccessful. Neutron scattering has revealed lamellar arrangements in comparably thin PFSA layers (*37*, *40*, *41*).

Seeking to characterize the CIPH and the ionomer configuration in its hydrated condition, we designed a suite of ex situ and in situ surface-enhanced Raman spectroscopy (SERS) experiments (Fig. 2I and fig. S10). As-deposited ionomers on Ag catalysts exhibited strong characteristic signals at 733 cm^{-1} (characteristic of $-CF_2$ and C–C vibrations, table S5) and at

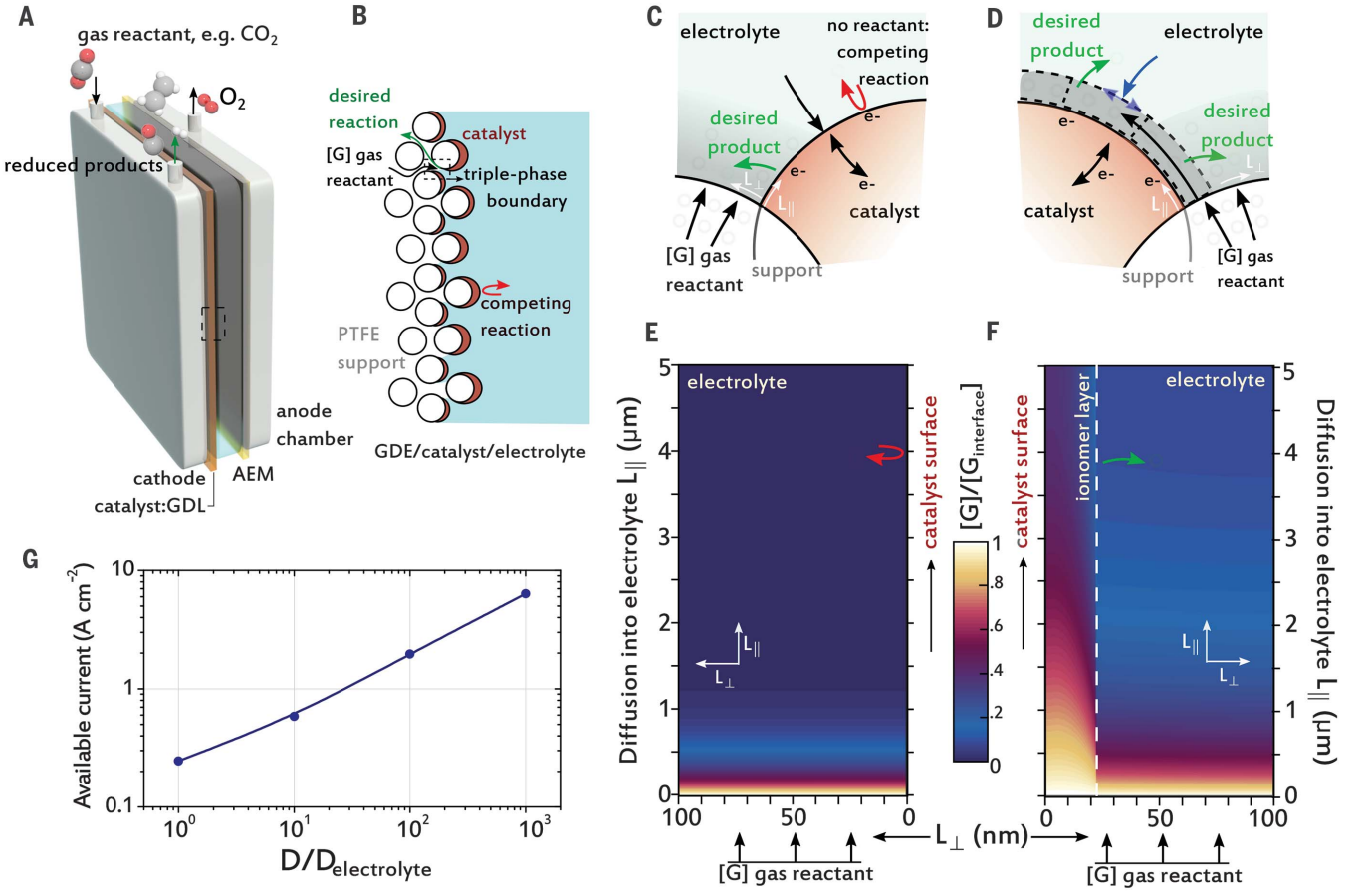

Fig. 1. Limiting current in gas-phase electrocatalysis and ionomer gas-liquid decoupled transport channels. (**A**) Flow-cell schematic. Reactant gases are fed through the back of a gas diffusion–electrode catalyst, facing an aqueous electrolyte. An anion-exchange membrane (AEM) facilitates OH^- transport from cathode to anode. GDL, gas-diffusion layer. (**B**) In a gas-diffusion electrode (GDE), catalysts are deposited onto a hydrophobic support from which gas reactants [G] diffuse. (**C**) The volume in which gas reactants, active sites, and water and ions coexist determines the maximum available current for gas electrolysis. Catalyst regions with limited reactant concentration promote by-product reactions such as hydrogen evolution. (**D**) When gas and electrolyte (water and ion source) transport is decoupled, the three-phase reaction interface can be extended so that all electrons participate in the desired electrochemical reaction. (**E** and **F**) Modeled gas reactant availability along the catalyst's surface for standard (E) and decoupled (F) gas transport into a 5 M KOH electrolyte, assuming an in-plane laminar gas diffusivity of $D_{||}/D_{KOH}$ = 1000 for the latter, where $D_{||}$ is gas diffusivity parallel to catalyst surface. Depending on the gas diffusivity within the gas transport channel, gas availability dramatically increases. $L_{||}$, distance parallel to catalyst surface; $L_\perp$, distance perpendicular to catalyst surface. (**G**) Modeled maximum available current density for CO_2 reduction. D/D_{KOH} manipulation enables entrance into the >1–A cm^{-2} regime for CO_2R. See methods for details on gas transport and reaction simulations.

1005 and 1130 cm^{-1} (associated with $-SO_3^-$ modes) as well as a complex background set of features arising from other C–C (1386 cm^{-1}), C–F (1182 and 1300 cm^{-1}), and S=O (1446 cm^{-1}) modes (*42*, *43*). Hydrated samples retain characteristic $-CF_2$, C–C and $-SO_3^-$ spectral features but a notably increased relative contribution of $-SO_3^-$ groups (1009 and 1131 cm^{-1}) compared with $-CF_2$ (730 cm^{-1}). This trend is maintained during operation in 1 M KOH electrolyte at −2 V versus Ag or AgCl reducing potentials and is also retained with the use of other catalyst metals such as Cu (fig. S11), suggesting that hydrated $-SO_3^-$ groups tend to face the electrocatalyst surface.

To assess the impact of the ionomer on gas availability, we evaluated the electrochemical performance of the CIPH for different metals and reactions in 5 M KOH electrolyte (Fig. 3). In the ORR, oxygen is reduced into water (*2*). The lack of a competing reaction to the ORR at potentials more positive than the hydrogen evolution reaction (HER) can be used to identify gas-reactant depletion and its impact on the limiting current. We built CIPH structures consisting of spray-cast ionomer coatings over PTFE/Ag substrates at different loadings, and we monitored the ORR current (fig. S12) using a 5 M KOH water electrolyte and air as reactants. Unmodified Ag catalysts showed a current density limited to less than 30 mA cm^{-2}. CIPH catalysts, on the other hand, exhibited a considerably enlarged current density that peaks at 250 mA cm^{-2} under the same conditions (Fig. 3A), with no H_2 production observed. In situ Raman measurements showed a consistent increase in the presence of O_2 near the catalyst surface at operating conditions (fig. S13). The observed enhancement can be explained as being due to ≈600× increased diffusion of O_2 relative to bulk electrolyte based on Knudsen diffusion of the reacting gas through CIPH hydrophobic domains (see methods).

To assess whether ion transport was modified in metal-ionomer catalysts, we compared the ORR and HER performance of standard Ag and Ag-CIPH samples for various electrolytes. Because the reactant in HER is in the aqueous phase (water or hydrated proton), the performance of the catalyst is not affected by the gas-diffusion properties of the PFSA ionomer layer; instead, catalyst performance is determined by water availability and ion transport. We found that CIPH samples exhibit similar hydrogen evolution activity to bare catalysts and increased ORR current across a wide range of electrolytes and pH (figs. S14 to S17). This result supports the notion that the enhanced ORR performance of the CIPH samples stems from extended gas transport.

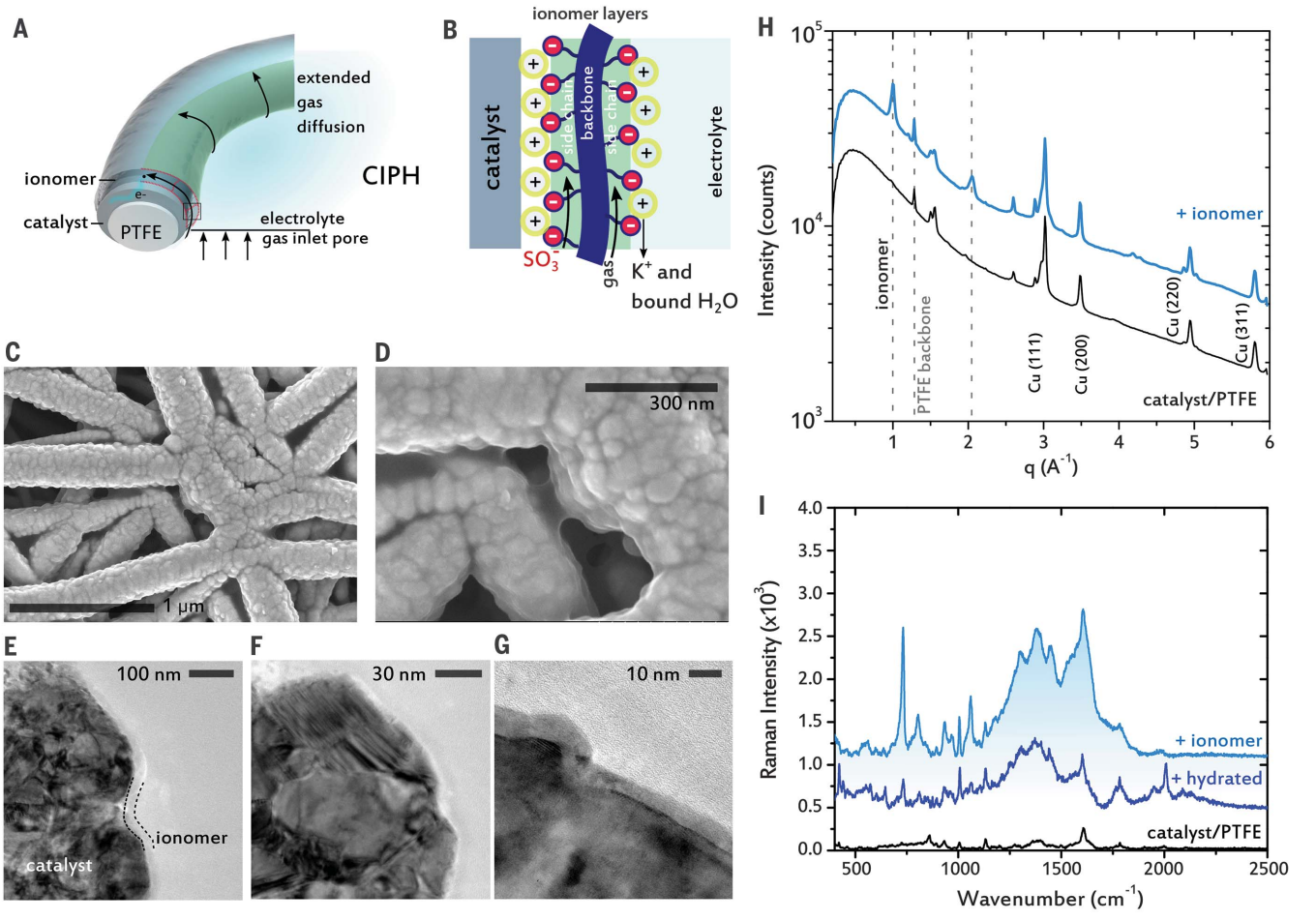

Fig. 2. The catalyst:ionomer planar heterojunction. (**A**) Schematic of metal catalyst deposited onto a PTFE hydrophobic fiber support. A flat ionomer layer conformally coats the metal. (**B**) Perfluorinated ionomers such as Nafion exhibit differentiated hydrophilic and hydrophobic characteristics endowed by $-SO_3^-$ and $-CF_2$ functionalities, respectively. Laminar Nafion arrangements have been reported depending on its thickness and substrate (*37*, *40*). (**C** and **D**) SEM images of ionomer-coated copper catalysts. (**E** to **G**) Cryo-microtomed TEM cross-sections of catalyst and ionomer revealing a laminar conformal overcoating. (**H**) WAXS spectra for reference and ionomer-modified catalysts. These reveal features at 1, 1.28, and 2 A^{-1}, associated with various PFSA and PTFE-support phases. (**I**) Raman spectra of reference and ionomer-modified catalysts revealing distinctive features of ionomer $-CF_2$ and $-SO_3^-$ groups (table S5).

We then focused on studying the performance of CIPH samples for CO_2 and CO reactants, investigating their reduction toward different products. We first screened Ag-CIPH samples for a CO_2 reduction reaction (CO_2RR) targeting CO production (*7*, *44*) and observed a CO_2RR partial current density of 400 mA cm^{-2} (Fig. 3B and fig. S18). By contrast, Ag reference samples, limited by CO_2 availability, exhibited a maximum CO_2RR partial current density of ≈54 mA cm^{-2}. This trend is maintained across different electrolytes (figs. S19 and S20).

These observations translate as well to Cu-CIPH catalysts targeting hydrocarbon generation (Fig. 3C and fig. S21) (*45*). Cu-CIPH catalysts exhibited a notable increase of CO_2RR current. At 800 mA cm^{-2}, H_2 generation remained below 10% Faradaic efficiency (FE), whereas the FE toward ethylene (C_2H_4) surpassed 60%. A CO_2 partial current density toward CO and ethylene of 510 mA cm^{-2} was achieved (Fig. 3C). Bare Cu catalysts, on the other hand, exhibited a limited CO_2RR current of 50 mA cm^{-2}. This performance is consistent with the increased presence of adsorbed CO intermediates, as observed using in situ Raman spectroscopy at similar conditions (fig. S13) (*46*). Based on the model presented herein, the observed enhancement can be explained by ≈400× increased diffusion of CO_2 relative to bulk electrolyte.

The electrochemical surface areas of reference and CIPH samples, as well as cell resistances, were comparable (see methods), indicating that these were not causes of the observed enhancement. These conclusions are further supported by the similar hydrophobicity of the catalysts before and after addition of the ionomer (fig. S8), consistent with the view that the enhanced gas reduction in CIPH samples originates from the extended gas diffusion through the ionomer layer, rather than from a redistribution of the gas or electrolyte in the PTFE substrate pores. Postreaction SEM revealed the unmodified presence of the PFSA ionomer in the CIPH after reaction (fig. S22).

To query the impact of CIPH when applied to other gas reactants, we monitored the CO reduction reaction (CORR) on Cu under similar reaction conditions—a system with activity limited by the poor solubility of CO in the electrolyte (Fig. 3D and fig. S23). Cu-CIPH samples yielded a CORR to ethylene partial current density of up to 340 mA cm^{-2}. Bare Cu samples, by contrast, showed a CORR limiting current of 64 mA cm^{-2}.

To study the effect of the ionomer on the kinetics of the reaction, which could lead to the difference in partial current densities observed, we carried out both ORR and CO_2RR in aqueous H-cell reactors. In this configuration, gas transport to the entire surface of the catalyst takes place through the electrolyte. In ORR, we observed a slight improvement in reaction kinetics, as indicated by a higher current density at low overpotential for CIPH

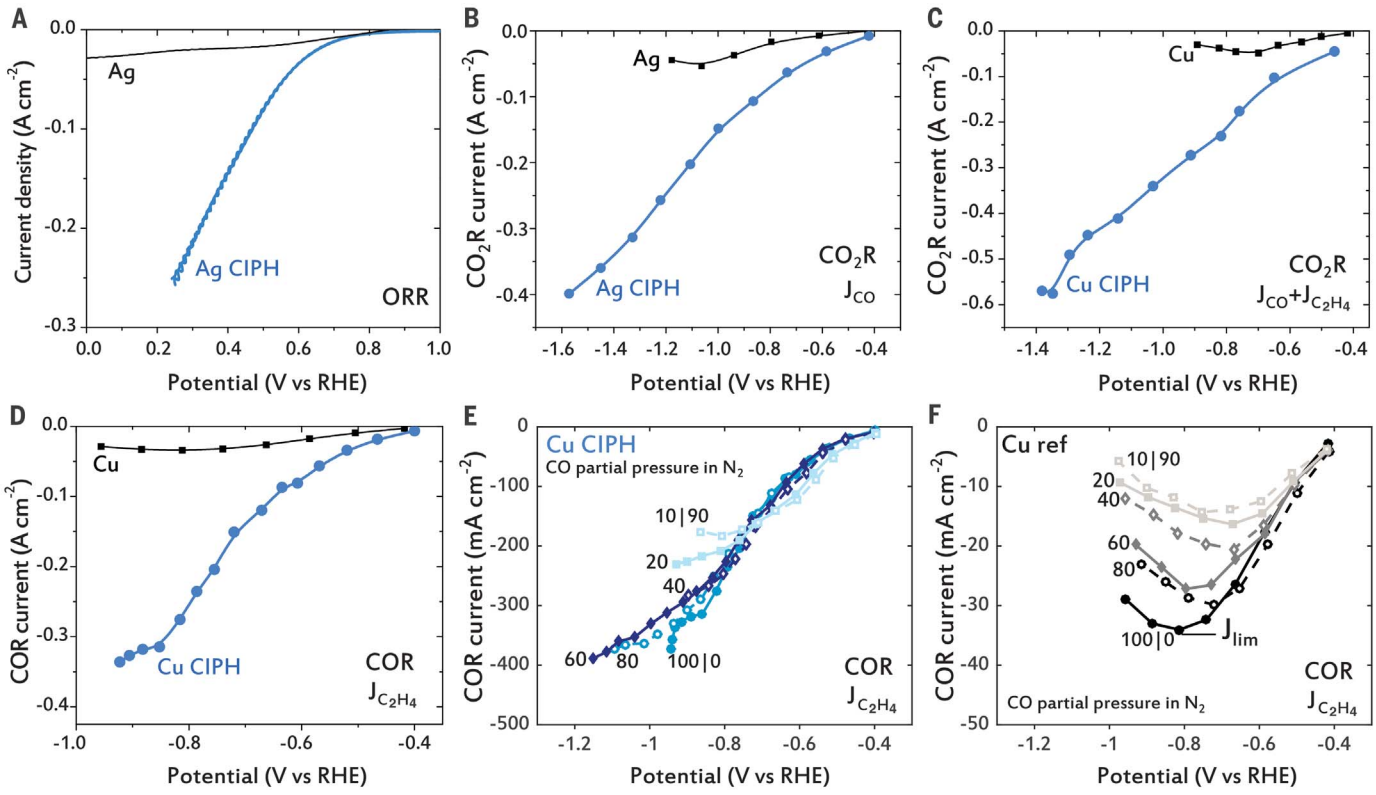

Fig. 3. Increased limiting current and underlying mechanisms for CIPH catalysts. (**A**) ORR showing a 30–mA cm^{-2} limiting current (J_{lim}) for Ag reference catalysts as opposed to 250 mA cm^{-2} for a CIPH configuration. RHE, reversible hydrogen electrode. (**B**) For CO_2RR, standard Ag catalysts yield a J_{lim} of ≈54 mA cm^{-2} (remaining current used for hydrogen evolution). This is in stark contrast with CIPH samples, which retain a FE above 85% for CO_2 reduction (CO_2R) to CO up to ≈500 mA cm^{-2}. (**C**) This trend is maintained for Cu CIPH catalysts and hydrocarbon production: J_{lim} toward ethylene (dominant product) is 50 mA cm^{-2} at −0.7 V versus RHE for bare Cu but increases beyond 0.5 A cm^{-2} for CIPH (peak FE of 61% at 835 mA cm^{-2}). (**D**) For CO reduction (COR), J_{lim} ≈ 64 mA cm^{-2} for standard Cu, whereas CIPH achieves a maximum 340–mA cm^{-2} current for the same reaction; H_2 by-product generation is restrained below 15% FE at all currents. (**E** and **F**) Partial pressure COR studies in $CO|N_2$ mixes for CIPH (E) and standard (F) catalyst show that only at partial pressures below 60% is J_{lim} observed for CIPH, whereas a sharp, steady decrease is observed for reference samples. At all partial pressures, CIPH exhibits an order of magnitude larger J_{lim}. Both reference and CIPH samples exhibit comparable resistance and double-layer capacitance. Electrochemical experiments were carried out in 5 M KOH electrolyte with a 50–cm^3 min^{-1} CO or CO_2 feedstock (in the case of 100% partial pressure).

samples (fig. S24). In CO_2RR on Ag-based catalyst, both bare Ag and Ag-CIPH showed comparable current densities (fig. S25), with a slight increase in CO FE (≈5%) for Ag-CIPH samples at low current density (<40 mA cm^{-2}), a finding attributable to a change in local environment induced by the Nafion layer. No change in oxidation or coordination number of the metal active sites was observed during in situ x-ray absorption spectroscopy (XAS) (fig. S26).

In the H-cell configuration, we observed similar limiting current densities for bare and CIPH samples in ORR and CO_2RR. These results indicate that although the presence of Nafion on the surface can change the reaction kinetics (*47*), it is its extended gas-transport properties that enable overcoming the limiting current density in gas-phase electrolysis.

To explore further the role of gas availability in the limiting current, we varied the gas availability by tuning the partial pressure of the reactant in N_2 mixtures (Fig. 3, E and F). A steep partial pressure dependence of limiting current density for ethylene was observed in CORR on Cu. Only at partial pressures below 60% was a limiting current observed for CIPH. At all CO partial pressures, Cu-CIPH exhibited an order of magnitude higher partial current density compared with bare Cu. We observed a similar trend in CO_2RR with varying CO_2 partial pressure (figs. S27 and S28). These results further confirm the role of the ionomer in enhancing reactant availability and thereby increasing current density.

In light of these findings, we sought to develop a catalyst design that took advantage of the gas-electrolyte segregated transport beyond two dimensions. Ideally, such a catalyst would maximize the triple-phase reaction interface across an extended three-dimensional (3D) morphology, enabling efficient operation in higher current regimes. We implemented a 3D catalyst:ionomer bulk heterojunction (CIBH) consisting of Cu nanoparticles and PFSA blended and spray-cast on a PTFE/Cu/ionomer (CIPH) gas-diffusion layer support, forming a 3D morphology with metal and ionomer percolation paths (Fig. 4A). Cross-sectional SEM

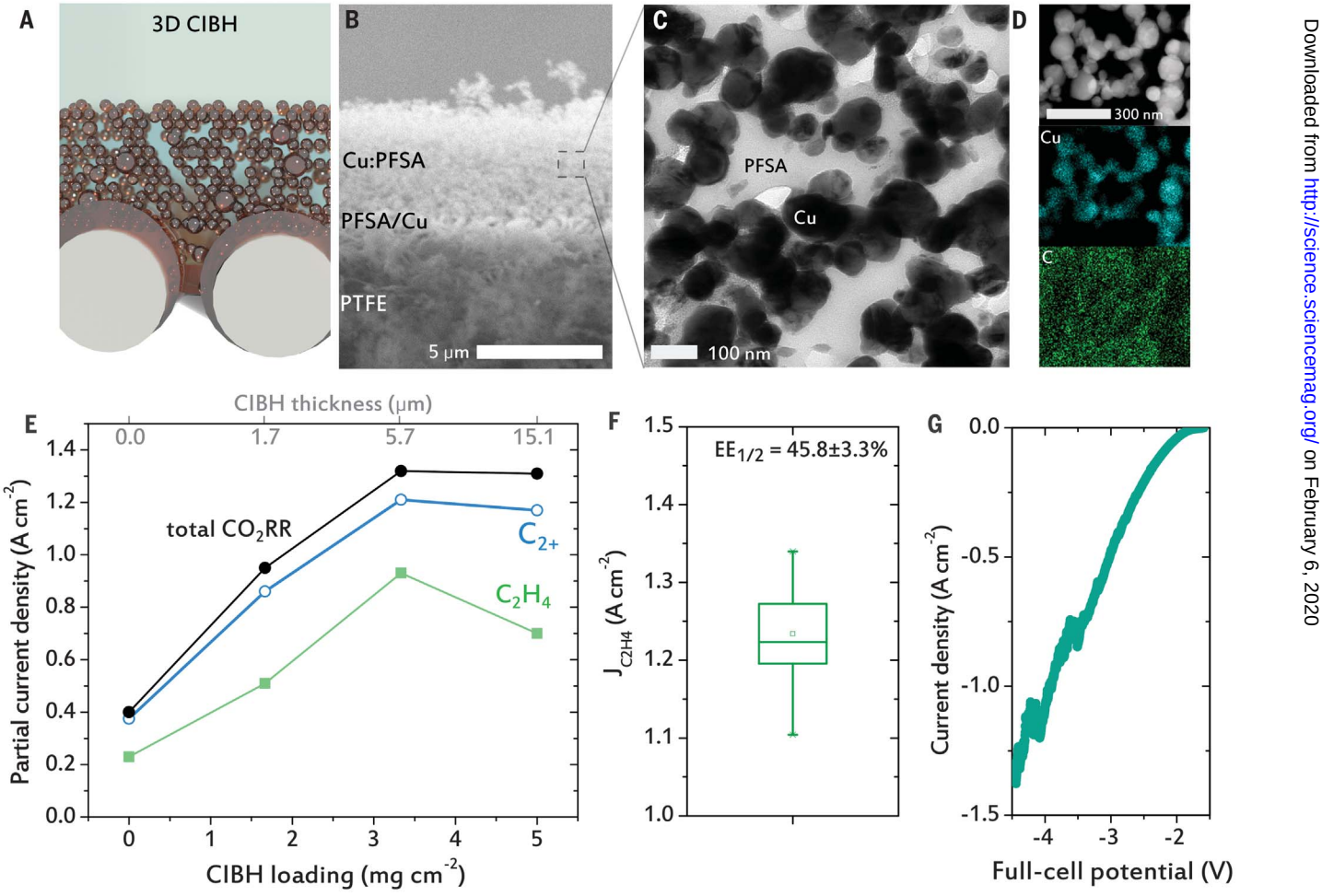

Fig. 4. 3D catalyst:ionomer bulk heterojunction for efficient gas-phase electrochemistry beyond 1 A cm^{-2}. (**A**) Schematic representation of metal-ionomer bulk heterojunction catalysts on a PTFE support. (**B**) Cross-sectional SEM of the CIBH catalyst. (**C** and **D**) TEM image of a cryo-microtomed CIBH (C) and elemental mapping of Cu and C revealing CIBH nanomorphology (D). (**E**) Partial current density for total CO_2RR reactions, with C_{2+} and C_2H_4 at maximum cathodic energy efficiency. The total CO_2R current saturates at 1.3 A cm^{-2} before cathodic energy efficiency drops for CIBH thicknesses beyond 6 µm. CIBH samples achieve more than a sixfold increase in partial current density at cathodic energy efficiencies >40% (fig. S30). Each sample and operating condition ran for at least 30 min. (**F**) Performance statistics of the highest partial current configuration for eight Cu CIBH catalysts. The box plot corresponds to Q1 to Q3 interquartile range, median, and average. The error bar represents ≈5.4 standard deviations. $EE_{1/2}$, half-cell (cathodic) energy efficiency. (**G**) Performance of the best CIBH catalyst in an ultraslim flow cell consisting of a 3-mm-wide catholyte channel. A full-cell energy efficiency of 20% for C_{2+} products is estimated at 1.1–A cm^{-2} operating current. All CIBH electrochemical experiments were carried out in 7 M KOH with a 50–cm^3 min^{-1} CO_2 feedstock.

images revealed the different layers in the CIBH catalyst (Fig. 4B). High-resolution cryomicrotomed cross-section images obtained using TEM and elemental energy-dispersive x-ray spectroscopy mapping further revealed the presence of continuous Cu nanoparticle and ionomer domains (Fig. 4, C and D).

We first optimized CIBH morphology by tuning the deposition conditions as well as the Cu:ionomer blend ratio, which we found optimized for a 4:3 weight/ by weight configuration. Using this configuration, with 7 M KOH electrolyte and 50 cm^3 min^{-1} of CO_2 flow, we then explored the effect of catalyst layer thickness. In an effective CIBH catalyst, CO_2RR current is expected to increase with catalyst loading until the length of the gas percolation paths through the ionomer phase reaches the gas reactant diffusion length. As we increased catalyst loading and corresponding thickness, we observed a monotonic increase in the total CO_2RR current, which surpassed 1 A cm^{-2} for a loading of 3.33 mg cm^{-2} (5.7 μm thickness) and which saturated at 1.32 A cm^{-2} for higher loadings before energy efficiency dropped (Fig. 4E). The total partial current for C_{2+} products (ethylene, ethanol, acetate, and propanol) reached 1.21 A cm^{-2} (fig. S29), which was achieved at a 45 ± 2% cathodic energy efficiency. The achieved C_{2+} partial current density represents a sixfold increase compared with previous best reports at similar energy efficiencies (*12*, *22*, *23*) (fig. S30 and tables S6 to S9).

The product distribution for optimal CIBH catalysts at different current densities in 7 M KOH electrolyte reveals that H_2 generation remains below 10% from 0.2 to 1.5 A cm^{-2} (fig. S29). At the highest current operation, optimized catalysts exhibited a maximum productivity toward ethylene with a FE in the 65 to 75% range, a peak partial current density of 1.34 A cm^{-2} at a cathodic energy efficiency of 46 ± 3% (Fig. 4F and figs. S31 and S32). We implemented the best CIBH catalyst in an ultraslim flow cell (with no reference electrode and a minimized catholyte channel of ≈3 mm, with water oxidized at a Ni foam anode), leading to an estimated full-cell energy efficiency toward C_{2+} products of 20% at 1.1 A cm^{-2} without the benefit of *iR* compensation (*i*, current; *R*, resistance) (Fig. 4G). CIBH catalyst current and FE remained stable over the course of a 60-hour initial study implemented in a membrane electrode assembly configuration (fig. S33).

Although CO_2 reduction kinetics improve with increasing temperature, alkaline electrolyzers manifest worsened CO_2 availability as temperature increases, and this fact curtails reaction productivity. We explored the effect of temperature on planar CIPH metal:ionomer catalysts and observed that CIPH catalysts require lower overpotentials to attain similar FE, in contrast with planar reference catalysts (fig. S34), when operated at 60°C. This effect translates into 3D CIBH catalysts, which show improved performance arising from the combination of accelerated CO_2 reduction kinetics and extended mass transport through the ionomer layer with increasing temperature (fig. S35). As a result, CIBH catalysts achieve ≈1 V reduced overpotential and more than a 50% increase in C_2 productivity when operated at industrial electrolyzer-relevant temperatures of 60°C in a full-cell configuration, compared with the case of room temperature operation (fig. S36).

The phenomena described herein showcase catalyst design principles that are not constrained by prior gas-ion-electron transport restrictions. The CIBH catalyst paves the way to the realization of renewable electrochemistry for hydrocarbon production at operating currents needed for industrial applications, as has been achieved with syngas for solid oxide electrolyzers (*48*, *49*).

REFERENCES AND NOTES

1. S. I. Seneviratne, M. G. Donat, A. J. Pitman, R. Knutti, R. L. Wilby, *Nature* **529**, 477–483 (2016).
2. Z. W. Seh *et al*., *Science* **355**, eaad4998 (2017).
3. S. Lin *et al*., *Science* **349**, 1208–1213 (2015).
4. C. Liu, B. C. Colón, M. Ziesack, P. A. Silver, D. G. Nocera, *Science* **352**, 1210–1213 (2016).
5. S. Verma, B. Kim, H.-R. M. Jhong, S. Ma, P. J. A. Kenis, *ChemSusChem* **9**, 1972–1979 (2016).
6. M. Jouny, W. Luc, F. Jiao, *Ind. Eng. Chem. Res.* **57**, 2165–2177 (2018).
7. Y. Hori, in *Modern Aspects of Electrochemistry* (Springer, 2008), pp. 89–189.
8. R. Kortlever, J. Shen, K. J. P. Schouten, F. Calle-Vallejo, M. T. M. Koper, *J. Phys. Chem. Lett.* **6**, 4073–4082 (2015).
9. Y. Zhang *et al*., *ACS Catal.* **7**, 4846–4853 (2017).
10. V. R. Stamenkovic, D. Strmcnik, P. P. Lopes, N. M. Markovic, *Nat. Mater.* **16**, 57–69 (2017).
11. M. L. Perry, J. Newman, E. J. Cairns, *J. Electrochem. Soc.* **145**, 5 (1998).
12. C.-T. Dinh *et al*., *Science* **360**, 783–787 (2018).
13. Y. Chen, C. W. Li, M. W. Kanan, *J. Am. Chem. Soc.* **134**, 19969–19972 (2012).
14. C. W. Li, J. Ciston, M. W. Kanan, *Nature* **508**, 504–507 (2014).
15. M. Liu *et al*., *Nature* **537**, 382–386 (2016).
16. Y. Lum, B. Yue, P. Lobaccaro, A. T. Bell, J. W. Ager, *J. Phys. Chem. C* **121**, 14191–14203 (2017).
17. S. Verma, X. Lu, S. Ma, R. I. Masel, P. J. A. Kenis, *Phys. Chem. Chem. Phys.* **18**, 7075–7084 (2016).
18. D. M. Weekes, D. A. Salvatore, A. Reyes, A. Huang, C. P. Berlinguette, *Acc. Chem. Res.* **51**, 910–918 (2018).
19. D. Higgins, C. Hahn, C. Xiang, T. F. Jaramillo, A. Z. Weber, *ACS Energy Lett.* **4**, 317–324 (2019).
20. M. Jouny, W. Luc, F. Jiao, *Nat. Catal.* **1**, 748–755 (2018).
21. K. Yang, R. Kas, W. A. Smith, *J. Am. Chem. Soc.* **141**, 15891–15900 (2019).
22. S. Ma *et al*., *J. Am. Chem. Soc.* **139**, 47–50 (2017).
23. J.-J. Lv *et al*., *Adv. Mater.* **30**, e1803111 (2018).
24. A. J. Martín, G. O. Larrazábal, J. Pérez-Ramírez, *Green Chem.* **17**, 5114–5130 (2015).
25. Z. Liu *et al*., *J. CO2 Util.* **15**, 50–56 (2016).
26. Y. Song, X. Zhang, K. Xie, G. Wang, X. Bao, *Adv. Mater.* **31**, 1902033 (2019).
27. T. Burdyny *et al*., *ACS Sustain. Chem.& Eng.* **5**, 4031–4040 (2017).
28. A. Kusoglu, A. Z. Weber, *Chem. Rev.* **117**, 987–1104 (2017).
29. T. D. Gierke, G. E. Munn, F. C. Wilson, *J. Polym. Sci., Polym. Phys. Ed.* **19**, 1687–1704 (1981).
30. K.-D. Kreuer, *Chem. Mater.* **8**, 610–641 (1996).
31. F. I. Allen *et al*., *ACS Macro Lett.* **4**, 1–5 (2015).
32. J.-P. Melchior, T. Bräuniger, A. Wohlfarth, G. Portale, K.-D. Kreuer, *Macromolecules* **48**, 8534–8545 (2015).
33. K.-D. Kreuer, G. Portale, *Adv. Funct. Mater.* **23**, 5390–5397 (2013).
34. M. Schalenbach *et al*., *J. Phys. Chem. C* **119**, 25145–25155 (2015).
35. L.-C. Weng, A. T. Bell, A. Z. Weber, *Phys. Chem. Chem. Phys.* **20**, 16973–16984 (2018).
36. R. Subbaraman, D. Strmcnik, V. Stamenkovic, N. M. Markovic, *J. Phys. Chem. C* **114**, 8414–8422 (2010).
37. S. C. DeCaluwe, A. M. Baker, P. Bhargava, J. E. Fischer, J. A. Dura, *Nano Energy* **46**, 91–100 (2018).
38. C.-H. Ma *et al*., *Polymer (Guildf.)* **50**, 1764–1777 (2009).
39. J. H. Lee *et al*., *Sci. Rep.* **8**, 10739 (2018).
40. S. C. DeCaluwe, P. A. Kienzle, P. Bhargava, A. M. Baker, J. A. Dura, *Soft Matter* **10**, 5763–5776 (2014).
41. A. Kusoglu *et al*., *Adv. Funct. Mater.* **24**, 4763–4774 (2014).
42. J. Zeng, D. I. Jean, C. Ji, S. Zou, *Langmuir* **28**, 957–964 (2012).
43. X. Ling, M. Bonn, S. H. Parekh, K. F. Domke, *Angew. Chem. Int. Ed.* **55**, 4011–4015 (2016).
44. C.-T. Dinh, F. P. García de Arquer, D. Sinton, E. H. Sargent, *ACS Energy Lett.* **3**, 2835–2840 (2018).
45. Y. Lum, J. W. Ager, *Nat. Catal.* **2**, 86–93 (2019).
46. M. C. Figueiredo, I. Ledezma-Yanez, M. T. M. Koper, *ACS Catal.* **6**, 2382–2392 (2016).
47. J. H. Lee *et al*., *Adv. Funct. Mater.* **28**, 1804762 (2018).
48. T. Burdyny, W. A. Smith, *Energy Environ. Sci.* **12**, 1442–1453 (2019).
49. J. Lu *et al*., *Sci. Adv.* **4**, eaar5100 (2018).
50. F. P. García de Arquer, Arquer_et_al_microscopies_aay4217.zip, figshare (2020); doi: 10.6084/m9.figshare.11406927.

ACKNOWLEDGMENTS

The authors thank D. Kopilovic and R. Wolowiec for electrochemical cell design and setup; Z. Wang and Y. Lum for assistance and useful discussions; the Ontario Centre for the Characterization of Advanced Materials (OCCAM) for sample preparation and characterization facilities; and T. P. Wu, Y. Z. Finfrock, G. Sterbinsky, and L. Ma for technical support at 9-BM beamline of APS. J.W. gratefully acknowledges financial support from the Ontario Graduate Scholarship (OGS) program. A.S. thanks Fonds de Recherche du Quebec–Nature et Technologies (FRQNT) for support in the form of a postdoctoral fellowship award. C.-T.D. and A.S. are currently affiliated with Queen's University and McGill University, respectively. Certain commercial equipment, instruments, or materials are identified in this paper in order to specify the experimental procedure adequately. Such identification is not intended to imply recommendation or endorsement by the National Institute of Standards and Technology, nor is it intended to imply that the materials or equipment identified are necessarily the best available for the purpose. **Funding:** This work was financially supported by the Ontario Research Foundation, Research Excellence Program; the Natural Sciences and Engineering Research Council (NSERC) of Canada; the CIFAR Bio-Inspired Solar Energy program; and TOTAL S.A. This research used resources of the National Synchrotron Light Source II, which is a U.S. Department of Energy (DOE) Office of Science Facility, operated at Brookhaven National Laboratory under contract no. DESC0012704, and synchrotron resources of the Advanced Photon Source (APS) (XAS measurements), an Office of Science User Facility operated for the U.S. DOE Office of Science by Argonne National Laboratory, and was supported by the U.S. DOE under contract no. DE-AC02-06CH11357 and the Canadian Light Source and its funding partners. **Author contributions:** A.R.K. is a guest researcher. F.P.G.d.A., C.-T.D., A.O., and J.W. designed and carried out all electrochemical experiments. F.P.G.d.A. and C.-T.D. designed all remaining experiments and characterizations. C.M. carried out diffusion-reaction simulations. C.G. and F.P.G.d.A. carried out Raman spectroscopies. A.S. carried out SEM imaging. A.R.K. performed WAXS measurements. J.E. carried out contact angle measurements. All authors discussed the results and assisted during manuscript preparation. F.P.G.d.A., C.-T.D., D.S., and E.H.S. supervised the project. **Competing interests:** F.P.G.d.A., C.-T.D., A.O., J.W., D.S., and E.H.S. have filed provisional patent application no. 62930229 regarding catalyst:ionomer devices. **Data and materials availability:** All data are reported in the main text and supplementary materials. Raw microscopy images are available at figshare (*50*).

SUPPLEMENTARY MATERIALS

science.sciencemag.org/content/367/6478/661/suppl/DC1
Materials and Methods
Figs. S1 to S36
Tables S1 to S9
References (*51*–*75*)

17 June 2019; resubmitted 22 September 2019
Accepted 23 December 2019
10.1126/science.aay4217

Science

CO_2 electrolysis to multicarbon products at activities greater than 1 A cm^{-2}

F. Pelayo García de Arquer, Cao-Thang Dinh, Adnan Ozden, Joshua Wicks, Christopher McCallum, Ahmad R. Kirmani, Dae-Hyun Nam, Christine Gabardo, Ali Seifitokaldani, Xue Wang, Yuguang C. Li, Fengwang Li, Jonathan Edwards, Lee J. Richter, Steven J. Thorpe, David Sinton and Edward H. Sargent

Science **367** (6478), 661-666.
DOI: 10.1126/science.aay4217

Graceful choreography for CO_2 and H_2O

One challenge for efficient electrochemical reduction of carbon dioxide (CO_2) is that the gas is hydrophobic, but many of its desirable reactions require water (H_2O). García de Arquer *et al.* addressed this problem by combining a copper electrocatalyst with an ionomer assembly that intersperses sulfonate-lined paths for the H_2O with fluorocarbon channels for the CO_2. The electrode architecture enables production of two-carbon products such as ethylene and ethanol at current densities just over an ampere per square centimeter.

Science, this issue p. 661

Science (print ISSN 0036-8075; online ISSN 1095-9203) is published by the American Association for the Advancement of Science, 1200 New York Avenue NW, Washington, DC 20005. The title *Science* is a registered trademark of AAAS.